



Defense Threat Reduction Agency  
8725 John J. Kingman Road, MS  
6201 Fort Belvoir, VA 22060-6201



DTRA-TR-15-21

# TECHNICAL REPORT

## Computational Fluid Dynamics Simulations of Inhaled Nano- and Micro-Particle Deposition in the Rhesus Monkey Nasal Passages

**Distribution Statement A.** Approved for public release; distribution is unlimited.

December 2016

DTRA01-03-D-0014

Jeffrey D. Schroeter et al.

Prepared by:  
Applied Research Associates,  
Inc.  
801 N. Quincy Street  
Suite 700  
Arlington, VA 22203

DESTRUCTION NOTICE:



Destroy this report when it is no longer needed.  
Do not return to sender.

PLEASE NOTIFY THE DEFENSE THREAT REDUCTION  
AGENCY, ATTN: DTRIAC/ J9STT, 8725 JOHN J. KINGMAN ROAD,  
MS-6201, FT BELVOIR, VA 22060-6201, IF YOUR ADDRESS  
IS INCORRECT, IF YOU WISH IT DELETED FROM THE  
DISTRIBUTION LIST, OR IF THE ADDRESSEE IS NO  
LONGER EMPLOYED BY YOUR ORGANIZATION.

<b>REPORT DOCUMENTATION PAGE</b>				<i>Form Approved</i> <i>OMB No. 0704-0188</i>	
<small>Public reporting burden for this collection of information is estimated to average 1 hour per response, including the time for reviewing instructions, searching existing data sources, gathering and maintaining the data needed, and completing and reviewing this collection of information. Send comments regarding this burden estimate or any other aspect of this collection of information, including suggestions for reducing this burden to Department of Defense, Washington Headquarters Services, Directorate for Information Operations and Reports (0704-0188), 1215 Jefferson Davis Highway, Suite 1204, Arlington, VA 22202-4302. Respondents should be aware that notwithstanding any other provision of law, no person shall be subject to any penalty for failing to comply with a collection of information if it does not display a currently valid OMB control number. <b>PLEASE DO NOT RETURN YOUR FORM TO THE ABOVE ADDRESS.</b></small>					
<b>1. REPORT DATE (DD-MM-YYYY)</b>		<b>2. REPORT TYPE</b>		<b>3. DATES COVERED (From - To)</b>	
<b>4. TITLE AND SUBTITLE</b>				<b>5a. CONTRACT NUMBER</b>	
				<b>5b. GRANT NUMBER</b>	
				<b>5c. PROGRAM ELEMENT NUMBER</b>	
<b>6. AUTHOR(S)</b>				<b>5d. PROJECT NUMBER</b>	
				<b>5e. TASK NUMBER</b>	
				<b>5f. WORK UNIT NUMBER</b>	
<b>7. PERFORMING ORGANIZATION NAME(S) AND ADDRESS(ES)</b>				<b>8. PERFORMING ORGANIZATION REPORT NUMBER</b>	
<b>9. SPONSORING / MONITORING AGENCY NAME(S) AND ADDRESS(ES)</b>				<b>10. SPONSOR/MONITOR'S ACRONYM(S)</b>	
				<b>11. SPONSOR/MONITOR'S REPORT NUMBER(S)</b>	
<b>12. DISTRIBUTION / AVAILABILITY STATEMENT</b>					
<b>13. SUPPLEMENTARY NOTES</b>					
<b>14. ABSTRACT</b>					
<b>15. SUBJECT TERMS</b>					
<b>16. SECURITY CLASSIFICATION OF:</b>			<b>17. LIMITATION OF ABSTRACT</b>	<b>18. NUMBER OF PAGES</b>  41	<b>19a. NAME OF RESPONSIBLE PERSON</b>
<b>a. REPORT</b>	<b>b. ABSTRACT</b>	<b>c. THIS PAGE</b>			<b>19b. TELEPHONE NUMBER (include area code)</b>

## UNIT CONVERSION TABLE

U.S. customary units to and from international units of measurement<sup>\*</sup>

U.S. Customary Units	Multiply by   Divide by <sup>†</sup>		International Units
<b>Length/Area/Volume</b>			
inch (in)	2.54	$\times 10^{-2}$	meter (m)
foot (ft)	3.048	$\times 10^{-1}$	meter (m)
yard (yd)	9.144	$\times 10^{-1}$	meter (m)
mile (mi, international)	1.609 344	$\times 10^3$	meter (m)
mile (nmi, nautical, U.S.)	1.852	$\times 10^3$	meter (m)
barn (b)	1	$\times 10^{-28}$	square meter (m <sup>2</sup> )
gallon (gal, U.S. liquid)	3.785 412	$\times 10^{-3}$	cubic meter (m <sup>3</sup> )
cubic foot (ft <sup>3</sup> )	2.831 685	$\times 10^{-2}$	cubic meter (m <sup>3</sup> )
<b>Mass/Density</b>			
pound (lb)	4.535 924	$\times 10^{-1}$	kilogram (kg)
unified atomic mass unit (amu)	1.660 539	$\times 10^{-27}$	kilogram (kg)
pound-mass per cubic foot (lb ft <sup>-3</sup> )	1.601 846	$\times 10^1$	kilogram per cubic meter (kg m <sup>-3</sup> )
pound-force (lbf avoirdupois)	4.448 222		newton (N)
<b>Energy/Work/Power</b>			
electron volt (eV)	1.602 177	$\times 10^{-19}$	joule (J)
erg	1	$\times 10^{-7}$	joule (J)
kiloton (kt) (TNT equivalent)	4.184	$\times 10^{12}$	joule (J)
British thermal unit (Btu) (thermochemical)	1.054 350	$\times 10^3$	joule (J)
foot-pound-force (ft lbf)	1.355 818		joule (J)
calorie (cal) (thermochemical)	4.184		joule (J)
<b>Pressure</b>			
atmosphere (atm)	1.013 250	$\times 10^5$	pascal (Pa)
pound force per square inch (psi)	6.984 757	$\times 10^3$	pascal (Pa)
<b>Temperature</b>			
degree Fahrenheit (°F)	[T(°F) – 32]/1.8		degree Celsius (°C)
degree Fahrenheit (°F)	[T(°F) + 459.67]/1.8		kelvin (K)
<b>Radiation</b>			
curie (Ci) [activity of radionuclides]	3.7	$\times 10^{10}$	per second (s <sup>-1</sup> ) [becquerel (Bq)]
roentgen (R) [air exposure]	2.579 760	$\times 10^{-4}$	coulomb per kilogram (C kg <sup>-1</sup> )
rad [absorbed dose]	1	$\times 10^{-2}$	joule per kilogram (J kg <sup>-1</sup> ) [gray (Gy)]
rem [equivalent and effective dose]	1	$\times 10^{-2}$	joule per kilogram (J kg <sup>-1</sup> ) [sievert (Sv)]

<sup>\*</sup> Specific details regarding the implementation of SI units may be viewed at <http://www.bipm.org/en/si/>.

<sup>†</sup> Multiply the U.S. customary unit by the factor to get the international unit. Divide the international unit by the factor to get the U.S. customary unit.

# CONTENTS

CONVERSION TABLE .....	iii
LIST OF FIGURES .....	v
LIST OF TABLES .....	vii
PREFACE .....	viii
SUMMARY .....	ix
1. INTRODUCTION .....	1
2. METHODS .....	3
3. RESULTS AND DISCUSSION .....	8
3.1. AIRFLOW SIMULATIONS .....	8
3.2. NASAL MICROPARTICLE DEPOSITION .....	9
3.3. NASAL NANOPARTICLE DEPOSITION .....	14
3.4. REGIONAL PARTICLE DEPOSITION .....	16
3.5. SEMI-EMPIRICAL NASAL DEPOSITION CURVES .....	22
4. CONCLUSIONS.....	26
5. WORKS CITED .....	27
DEFINITIONS, ACRONYMS, AND ABBREVIATIONS .....	30

## LIST OF FIGURES

Figure 2-1. 3D reconstructions of the adult (top) and infant (bottom) rhesus monkey nasal passages. Approximate locations of olfactory (dark grey) and squamous (black) epithelium are identified. The larynx/trachea region (dark grey) is identified in the infant model. Image sizes are not to scale. ....	3
Figure 2-2. Cross-sectional areas in the adult and infant rhesus monkey nasal models as a function of normalized distance from the nostrils to the nasopharynx. ....	6
Figure 3-1. Steady-state inspiratory airflow streamlines at twice minute volume. Adult monkey: 7.4 L/min; infant monkey: 617 ml/min. Maximum airflow velocities are 5 m/sec. ....	8
Figure 3-2. Transnasal pressure drop (Pa) versus steady inspiratory flow rate (L/min) in the adult and infant monkey nasal CFD models and the adult monkey nasal molds from Kelly et al. (2005) and Yeh et al. (1990). ....	9
Figure 3-3. Microparticle nasal deposition predictions in the monkey nasal models as a function of particle size - adult model. ....	10
Figure 3-4. Microparticle nasal deposition predictions in the monkey nasal models as a function of particle size - infant model. ....	10
Figure 3-5. Microparticle nasal deposition predictions in the adult and infant monkey nasal models as a function of the impaction parameter. Deposition data from an adult rhesus monkey nasal cast is included (Kelly et al., 2005). ....	11
Figure 3-6. Total nasal deposition results of inhaled microparticles in the adult and infant monkey nasal models as a function of Stokes number. Various forms of the hydraulic diameter were used in Stokes number calculations: $4 \cdot A_{\text{nostril}} / P_{\text{nostril}}$ ....	12
Figure 3-7. Total nasal deposition results of inhaled microparticles in the adult and infant monkey nasal models as a function of Stokes number. Various forms of the hydraulic diameter were used in Stokes number calculations: $2\sqrt{V / \pi L}$ ....	12
Figure 3-8. Total nasal deposition results of inhaled microparticles in the adult and infant monkey nasal models as a function of Stokes number. Various forms of the hydraulic diameter were used in Stokes number calculations: $4 \cdot \text{SAVR}^{-1}$ ....	13
Figure 3-9. Total nasal deposition results of inhaled microparticles in the adult and infant monkey nasal models as a function of Stokes number. Various forms of the hydraulic diameter were used in Stokes number calculations: $\sqrt{4A_{cs} / \pi}$ ....	13

Figure 3-10. Comparison of nanoparticle deposition predictions in the adult rhesus monkey nasal CFD model with the experimental measurements of Yeh et al. (1992).....	14
Figure 3-11. Nanoparticle nasal deposition predictions in the adult and infant monkey nasal CFD models. ....	15
Figure 3-12. Nanoparticle nasal deposition predictions in the adult and infant monkey nasal CFD models as a function of the diffusion parameter, $d$ . The characteristic diameter was $d_c = 2\sqrt{V / \pi L}$ .....	16
Figure 3-13. Total nasal deposition predictions in the monkey nasal CFD models: adult. ....	17
Figure 3-14. Total nasal deposition predictions in the monkey nasal CFD models: infant.....	17
Figure 3-15. Deposition predictions on squamous epithelium in the monkey nasal passages: adult. ....	18
Figure 3-16. Deposition predictions on squamous epithelium in the monkey nasal passages: infant. ....	18
Figure 3-17. Deposition predictions on olfactory epithelium in the monkey nasal passages: adult. ....	19
Figure 3-18. Deposition predictions on olfactory epithelium in the monkey nasal passages: infant. ....	20
Figure 3-19. Deposition predictions on respiratory/transitional epithelium in the monkey nasal passages: adult. ....	21
Figure 3-20. Deposition predictions on respiratory/transitional epithelium in the monkey nasal passages: infant.....	21
Figure 3-21. Deposition predictions in the larynx/trachea region in the infant monkey nasal CFD model. ....	22
Figure 3-22. Empirical curve for nasal deposition of microparticles as a function of the impaction parameter. Data points represent CFD simulations results from the infant monkey model. ....	23
Figure 3-23. Empirical curves for nasal deposition of nanoparticles as a function of the diffusion parameter. Data points represent CFD simulation results from the infant monkey model. ....	24

## LIST OF TABLES

Table 2-1. Geometric measurements from the monkey nasal models .....	4
Table 2-2. Characteristic diameters (mm) used in the Stokes number calculations. ....	6
Table 3-1. Optimized parameter values for the sigmoidal functions for nasal deposition by inertial impaction ( $\eta_i$ ) and diffusion ( $\eta_d$ ). ....	24



## **PREFACE**

The research work described in this report was conducted for the Defense Threat Reduction Agency (DTRA) under contract number DTRA01-03-D-0014-0030. The Contract Officer's Representative for this effort was Mr. Rick Fry of DTRA's Information Systems Capability Development Office (J9CBI).

## SUMMARY

Anatomically accurate computational fluid dynamics (CFD) models of the nasal passages of an infant (6 months old, 1.3 kg) and adult (7 years old, 11.9 kg) rhesus monkey were used to predict deposition of inhaled nano- and micro-particles. Steady-state, inspiratory airflow simulations were conducted in each model at flow rates equal to 100%, 200%, and 300% of the estimated minute volume for resting breathing. Particle transport and deposition simulations were conducted using the Lagrangian method to track the motion of individual particles that were passively released from the nostrils. Particle deposition fractions were higher in the infant model than the adult model at equivalent physiological flow rates. However, deposition curves collapsed when accounting for differences in nasal geometry by plotting microparticle deposition against the Stokes number and nanoparticle deposition as a function of the Schmidt number and diffusion parameter. Particle deposition was also quantified on major nasal epithelial types. Maximum olfactory deposition ranged from 5-14% for 1-2 nm particles in the adult and infant models, depending on flow rate. For these particle sizes, deposition on respiratory/transitional epithelia ranged from 40-50%. Increased deposition was also predicted for olfactory and respiratory/transitional epithelia for particle sizes  $> 5 \mu\text{m}$  in the infant model and  $> 8 \mu\text{m}$  in the adult model. Semi-empirical curves for nasal deposition were developed based on the simulation data for nano- and micro-particle deposition to allow for simplified calculations of age-based nasal deposition in the rhesus monkey nasal passages that can be implemented into lung dosimetry models.

# 1. INTRODUCTION

Assessment of human health risks from exposure to inhaled materials often relies on extrapolation of dose-response data from laboratory animals. Nonhuman primates are frequently used in inhalation toxicology studies due to their similarities in respiratory tract structure to humans (Desso, 1993; Hislop et al., 1984; Harkema, 1991). Monkeys have been used to assess effects from inhalation of reactive gases such as ozone, chlorine and formaldehyde (Carey et al., 2007; Klonne et al., 1987; Monticello et al., 1989), diesel exhaust and coal dust (Nikula et al., 1997), metal particles (Dorman et al., 2006; Griffin et al., 1975), and infectious biological agents (Day and Berendt, 1972; Druett et al., 1953), to name a few examples. During resting breathing, the nasal passages serve as the primary entryway for inhaled particles and gases and are therefore at risk of insult from their deposition. An accurate quantification of regional dose to the epithelial cells lining the nose is critical in determining the exposure-dose-response behavior in monkeys and evaluating subsequent risk for humans via extrapolation.

Even though monkeys and humans share many commonalities, there are differences in airway morphology that affect the deposition of inhaled materials. Many studies have been conducted to quantify nasal particle deposition in humans, and several studies have been conducted to determine how differences in particle size affect nasal deposition and subsequent responses in monkeys. Kelly et al. (2005) used a replica cast of the nasal airways of an adult rhesus monkey to measure the deposition efficiency of particles in the 1- 10  $\mu\text{m}$  size range and found that deposition increased with flow rate and particle size. Yeh et al. (1992) also used a replica cast to measure the deposition efficiency of nanoparticles in the 5 – 200 nm size range. Nanoparticle deposition was also measured in vivo by Yeh et al. (1997) in adult rhesus monkeys and their results agreed well with the replica cast data, showing that deposition increased as nanoparticle size decreased. Cheng et al. (2008) measured respiratory deposition of 2 and 5  $\mu\text{m}$  droplets in cynomolgus monkeys and observed higher extrathoracic airway deposition at the larger particle size (58% versus 39%).

Particle size effects were also noted following exposure to infectious agents. In the study by Day and Berendt (1972), respiratory tract responses in monkeys exposed to aerosol particles containing tularemia (*Pasteurella tularensis*) differed depending on the particle size. Animals exposed to 2.1 or 7.5  $\mu\text{m}$  particles displayed lung congestion upon necropsy, whereas effects in animals exposed to 12.5 or 24  $\mu\text{m}$  particles were confined to the upper respiratory tract. They also found that as particle size increased, an increase in dose was required to initiate a lethal infection. In the study by Harper and Morton (1953), monkeys exposed to aerosolized spores of anthrax (*Bacillus anthracis*) showed increased head retention as particle size increased from 1 to 12  $\mu\text{m}$ . Furthermore, Druett et al. (1953) reasoned that the site and level of infection was dependent on particle size after exposing monkeys to 12  $\mu\text{m}$  diameter or single-spore anthrax particles.

Experimental studies have provided invaluable data on the effects of particle size on respiratory deposition characteristics, yet each study is limited by the number of animals exposed and is typically confined to a narrow particle size range. Computational fluid dynamics (CFD) models allow for simulation of airflow patterns and particle deposition efficiencies in complex geometries such as those found in the upper respiratory tract of laboratory animals and humans and provide a valuable supplement to experimental work in evaluating dose-response behavior. CFD models have been

developed to study airflow, gas uptake and particle deposition in multiple species, including rats, dogs, and humans (e.g., Ghalati et al., 2012; Kimbell et al., 1997; Jiang and Zhao, 2010; Lawson et al., 2012; Schroeter et al., 2012). There have also been several CFD studies on vapor uptake of inhaled chemicals in monkeys. Kepler et al. (1998) developed a CFD model of the adult rhesus monkey nasal passages to study airflow and formaldehyde uptake. This model was subsequently used by Kimbell et al. (2001) to compare formaldehyde flux patterns in rats, monkeys, and humans. Corley et al. (2012) used a CFD model of the upper and lower respiratory tract of an infant rhesus monkey to study uptake of inhaled acrolein vapor. While there have been a couple efforts modeling lung deposition of inhaled particles in monkeys (Agharian et al., 2012; Martonen et al., 2001), there have not been any CFD studies to date that quantify the deposition of inhaled particles in the upper respiratory tract of monkeys. Nasal particle filtration is important to understand to be able to predict localized dose to the nasal epithelium and to quantify the fraction of inhaled particles that reach the lung.

In this study, CFD models of the nasal passages of an adult and infant rhesus monkey (*Macaca mulatta*) were used to simulate inhaled airflow and particle deposition. Total and epithelial deposition fractions were quantified for inhaled nanoparticles (0.5-1000 nm) and microparticles (1-20  $\mu\text{m}$ ). Semi-empirical curves were developed based on the simulation results to extrapolate nasal deposition to other exposure conditions and to allow estimation of nasal filtration for rhesus monkey lung dosimetry models.

## 2. METHODS

Nasal airflow models were developed for an adult (7-year old male, 11.9 kg) and infant (6-month old male, ~1.3 kg) rhesus monkey (Figure 2-1). The reconstruction of the adult model was originally developed by Kepler et al. (1998) from serial Magnetic Resonance Imaging (MRI) sections of the right nasal passages (nostril to nasopharynx).



**Figure 2-1. 3D reconstructions of the adult (top) and infant (bottom) rhesus monkey nasal passages. Approximate locations of olfactory (dark grey) and squamous (black) epithelium are identified. The larynx/trachea region (dark grey) is identified in the infant model. Image sizes are not to scale.**

For this study, the original numerical mesh developed by Kepler and colleagues that was comprised of hexahedral elements was removed and the surface mesh was refined and smoothed to generate more anatomically realistic surface contours of the nasal passages. The infant rhesus monkey model was originally developed by Corley et al. (2012) and was based on Computed Tomography (CT) imaging of the upper airways and MRI imaging of a lung cast to form a contiguous reconstruction from the nostrils through 19 airway generations of the lung. For this study, the model developed by Corley and colleagues was truncated midway through the trachea to focus on particle deposition in the upper respiratory tract (Figure 2-1). The major nasal epithelial types consisting of squamous and olfactory epithelia were

mapped onto the surface mesh of each model according to the definitions from Carey et al. (2007) and Kimbell et al. (2001) (see Figure 2-1 and Table 2-1). The remaining surface is composed of transitional and respiratory epithelium.

**Table 2-1. Geometric measurements from the monkey nasal models**

Region	Adult model	Infant model
Surface area (mm <sup>2</sup> )		
Whole nose	7588.6	2019.7 <sup>a</sup>
Squamous	899.2	204.8
Olfactory	979.2	331.2
Larynx/Trachea	N/A	458.2
Volume (mm <sup>3</sup> )	7675.2	1110.7
Length (mm) <sup>b</sup>	75.5	41.4
A <sub>cs</sub> (mm <sup>2</sup> ) <sup>c</sup>	142.5	39.2
Area of nostrils (mm <sup>2</sup> )	88.8	11.9
Perimeter of nostrils (mm)	53.8	23.8

<sup>a</sup>excludes larynx/trachea surface area

<sup>b</sup>length from the tip of the nares to the back of the nasopharynx

<sup>c</sup>coronal cross-sectional area of the airway lumen at the beginning of the middle turbinate

Numerical meshes were generated in each model using ICEM-CFD™ (ANSYS, Inc.). Each mesh consisted of unstructured tetrahedral elements with a thin 3-layer boundary of prism elements along airway walls. The adult and infant monkey nasal models contained 5.8 and 7.9 million elements, respectively.

Steady-state, laminar inspiratory airflow simulations were conducted using Fluent™ (ANSYS, Inc.) to solve the viscous, incompressible Navier-Stokes equations. The segregated algorithm was used to solve the continuity and momentum equations; the SIMPLEC method was used for pressure-velocity coupling; a second order scheme was used to solve for pressure; and a second-order upwind scheme was used to solve the momentum equations. Airflow simulations were conducted with a density of 1.204 kg/m<sup>3</sup> and a dynamic viscosity of 1.8 x 10<sup>-5</sup> kg/m-sec. Boundary conditions in the nasal CFD models consisted of a pre-defined mass flow condition at the nostril(s), zero pressure at the outlet, and a no-slip condition on all airway walls. Airflow simulations were conducted at the minute volume (MV), twice the minute volume (2MV), and three times the minute volume (3MV) to span a range of physiological breathing rates. Minute volumes were estimated using the allometric formula from Bide et al. (2000):

$$MV = 0.499BW^{0.809},$$

where  $MV$  = minute volume (L/min) and  $BW$  = body weight (kg). Using this formula, minute volumes for the adult and infant monkeys were estimated to be 3.7 L/min and 617 ml/min, respectively. Airflow simulations were therefore conducted at flow rates of 1.85, 3.7, and 5.55 L/min in the adult model (flow rates reflect half the whole-nose flow rates since the adult model consisted of only one side of the nose) and 617, 1234, and 1851 ml/min in the infant nasal model. Reynolds numbers at the nostrils were 307, 614, and 921 in the adult model and 116, 232, and 348 in the infant model at the respective flow rates, thereby justifying the use of a laminar model for inhaled airflow.

Particle trajectories were calculated using the Discrete Phase Model in Fluent<sup>TM</sup> to solve the Lagrangian equations of motion which were decoupled from the flow field. Particle transport is a function of the drag force, gravity, and for submicron particles also includes diffusion effects due to Brownian motion. The Brownian force was modeled by a Gaussian white-noise random process model (Li and Ahmadi, 1992) and was implemented with user-defined functions in Fluent to improve upon the default methods for modeling deposition of submicron particles. Further details of the solution procedures for particle trajectories can be found in Schroeter et al. (2012).

Uniform concentrations of monodisperse particles with a density of 1.0 g/cm<sup>3</sup> were passively released from the nostril(s). Particle sizes of 1 nm to 20  $\mu$ m were simulated. Nasal airway walls were defined to be perfectly absorbing. Deposition fractions for the whole nose and epithelial-specific (squamous, olfactory, and respiratory/transitional) regions were computed by dividing the number of particles deposited by the number of particles released. Submicron particle deposition fractions were computed from the average of five independent simulations.

Microparticle deposition predominantly occurs by inertial impaction due to the high airflow velocities and narrow airway channels present in the nasal passages. In the inertial regime, deposition results can be characterized by the impaction parameter (IP), which is a function of aerodynamic diameter and flow rate:

$$IP = \rho d^2 Q$$

where  $\rho$  is the particle density,  $d$  is the particle diameter, and  $Q$  is the inhalation flow rate. However, the impaction parameter does not account for different geometric conditions when comparing results from models that are similar in shape but have different overall dimensions. Instead, the Stokes number is commonly used to compare inertial deposition predictions from multiple models since it includes terms for the characteristic diameter and velocity. The Stokes number can be written as

$$Stk = \frac{\rho d^2 U}{18 \mu d_c},$$

where  $U$  is the characteristic airflow velocity,  $\mu$  is the dynamic viscosity, and  $d_c$  is a characteristic diameter. Assuming the monkey nasal passages retain their general shape but grow in size with age, microparticle deposition was compared in the adult and infant monkey nasal models through the use of the Stokes number where the characteristic diameter was calculated for each model. Various forms of the characteristic diameter were investigated based on geometric measurements of the models and are

summarized in Table 2-2. These included setting the characteristic diameter equal to the hydraulic diameter at the nostrils, which assumes that variability in deposition can be attributed to differences in entrance effects, computing the diameter from the volume and length scales of the models (Grgic et al., 2004), and defining the diameter in terms of the surface area to volume ratio. We also investigated the characteristic diameter defined in terms of the cross-sectional area. Although Cheng (2003) proposed using the minimal cross-sectional area, a minimum value was not apparent from our cross-sectional area calculations in the monkey nasal models (Figure 2-2), so the characteristic diameter was computed using the cross-sectional area at the beginning of the middle turbinate in both models. All geometric measurements were calculated from the numerical mesh using ICEM-CFD<sup>TM</sup> (ANSYS, Inc.).

**Table 2-2. Characteristic diameters (mm) used in the Stokes number calculations.**

Characteristic Diameter	Adult model	Infant model
$4 \cdot A_{\text{nostril}} / P_{\text{nostril}}$	6.60	2.00
$2\sqrt{V / \pi L}$	11.40	5.85
$4 \cdot \text{SAVR}^{-1}$	4.05	2.21
$\sqrt{4A_{\text{cs}} / \pi}$	13.5	7.07

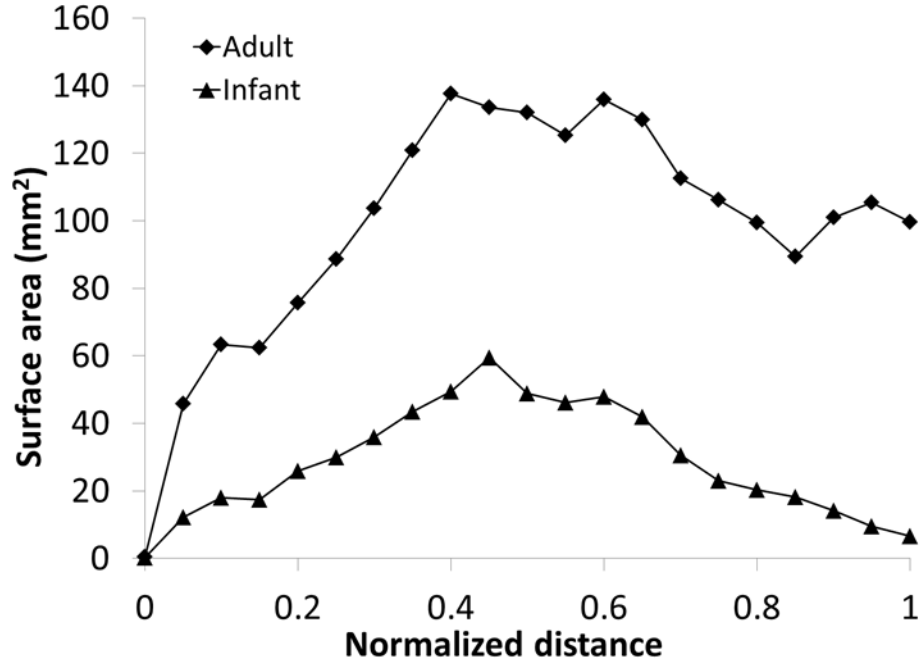


**Figure 2-2. Cross-sectional areas in the adult and infant rhesus monkey nasal models as a function of normalized distance from the nostrils to the nasopharynx.**



For nanoparticles, which primarily deposit by diffusion, Ingham (1991) showed that deposition can be quantified in terms of the diffusion parameter,  $\Delta$ , and the Schmidt number,  $Sc$ . The diffusion parameter is defined as:

$$\Delta = \frac{L}{Pe \cdot d_c},$$

where  $L$  is a characteristic length and  $Pe$  is the Peclet number, defined as

$$Pe = \frac{d_c U}{D}.$$

$D$  is the molecular diffusivity of particles in air and can be calculated from the Stokes-Einstein equation (Hinds, 1999). The Schmidt number is defined as

$$Sc = \frac{\nu}{D},$$

where  $\nu$  is the kinematic viscosity of air. The characteristic diameters defined above were used to calculate diffusion parameters for comparison of nanoparticle deposition results between the adult and infant monkey models.

### 3. RESULTS AND DISCUSSION

#### 3.1. AIRFLOW SIMULATIONS

Steady-state inspiratory airflow simulations were conducted in the adult and infant monkey models. Airflow patterns were similar to the results from Kepler et al. (1998) and were characterized by some swirling flow in the vestibule and streamlined flow in the central nasal passages (Figure 3-1). At flow rates equal to twice minute volume, maximum airflow velocities were approximately 3-4 m/sec in the vestibule and decreased to 1-3 m/sec in the central nose. The highest airflow velocities occurred in the nasopharyngeal region where the airway diameters narrowed (Figure 3-1). The fraction of inspiratory airflow directed to the olfactory region was approximately 22% in both models.

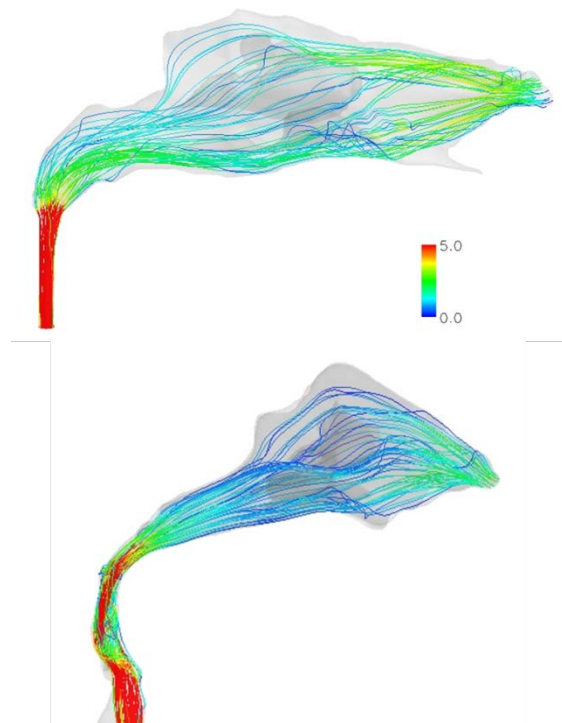


**Figure 3-1. Steady-state inspiratory airflow streamlines at twice minute volume. Adult monkey: 7.4 L/min; infant monkey: 617 ml/min. Maximum airflow velocities are 5 m/sec.**

The pressures at the nostril(s) and the nasopharyngeal outlet were computed to calculate the pressure gradient across each nasal model under steady airflow conditions (Figure 3-2). Pressure drop as a function of flow rate in the adult model fell between the pressure-flow curves from two other studies that measured pressure drop in adult monkey nasal replica casts (Kelly et al., 2005; Yeh et al., 1992). At equivalent flow rates, pressure drops in the infant model were significantly larger than the adult model due to narrower airways in the smaller model contributing more resistance to airflow.

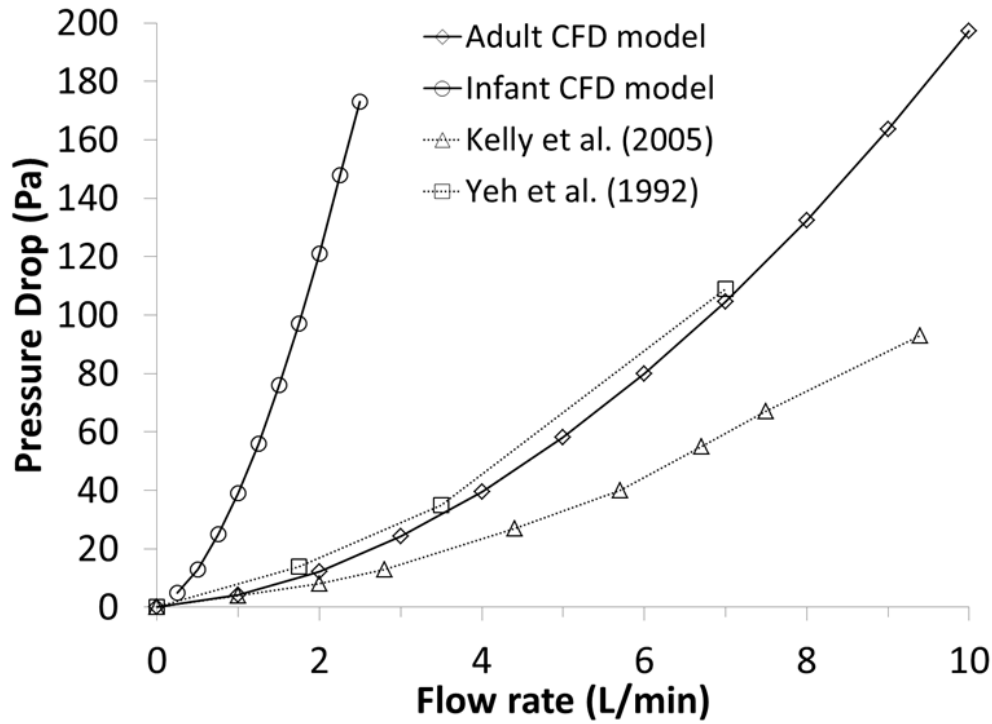


**Figure 3-2. Transnasal pressure drop (Pa) versus steady inspiratory flow rate (L/min) in the adult and infant monkey nasal CFD models and the adult monkey nasal molds from Kelly et al. (2005) and Yeh et al. (1990).**

### 3.2. NASAL MICROPARTICLE DEPOSITION

Deposition of microparticles in the rhesus monkey nasal passages displayed sigmoidal shapes with estimated deposition fractions near 1% for 1  $\mu\text{m}$  particles and increasing with particle size (Figure 3-3 and Figure 3-4). At twice minute volume, nasal deposition reached 100% at particle sizes of 14  $\mu\text{m}$  and 9  $\mu\text{m}$  in the adult and infant models, respectively. At equivalent physiological flow rates, deposition was higher in the infant model for all particle sizes. Higher nasal deposition was observed at higher flow rates due to increased inertial effects. When deposition was plotted against the impaction parameter, deposition curves from multiple flow rates collapsed for each model, signifying the effects of inertial impaction on deposition (Figure 3-5). Deposition values in the adult model were slightly lower than the data from Kelly et al. (2005). This discrepancy can partially be attributed to the fact that the adult CFD model used in this study did not contain a larynx or trachea which would result in less deposition, and may also be due to inter-subject variability between the two models. Deposition in the infant model was significantly higher than the data from Kelly et al. (2005) due to the smaller model size.

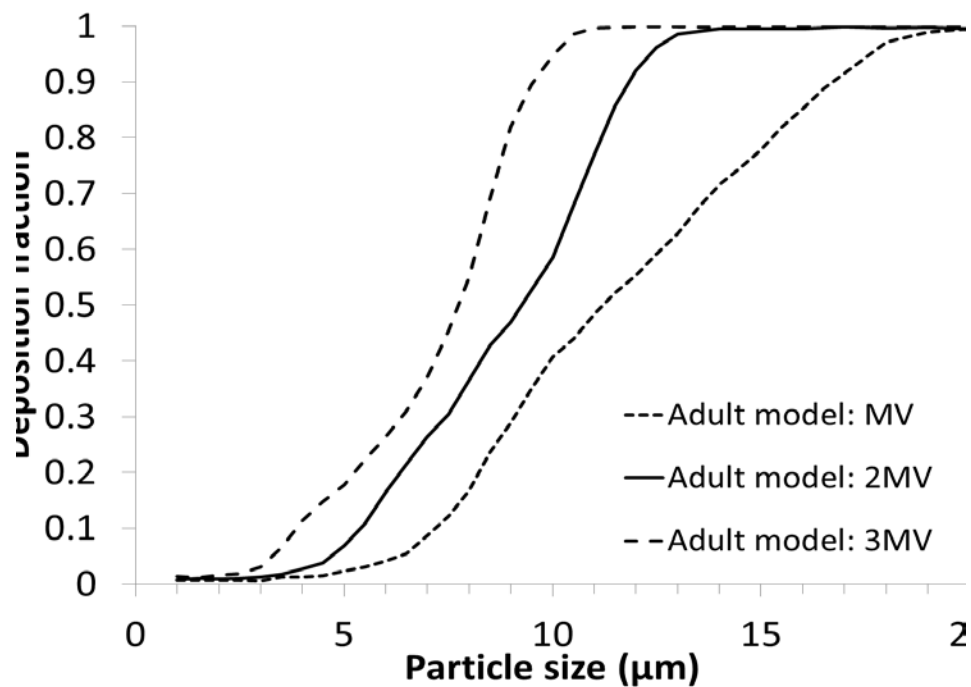


Figure 3-3. Microparticle nasal deposition predictions in the monkey nasal models as a function of particle size - adult model.

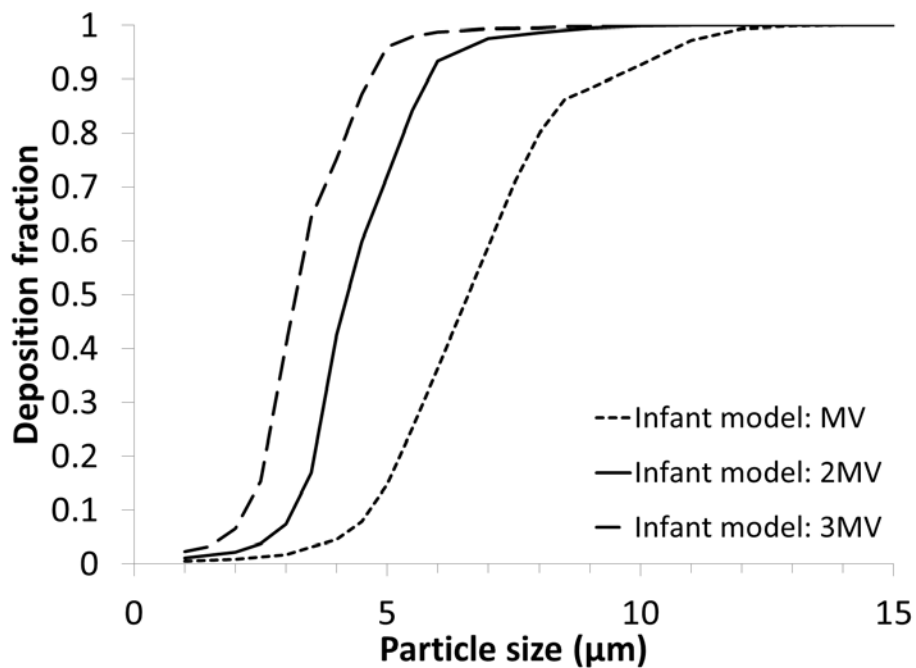
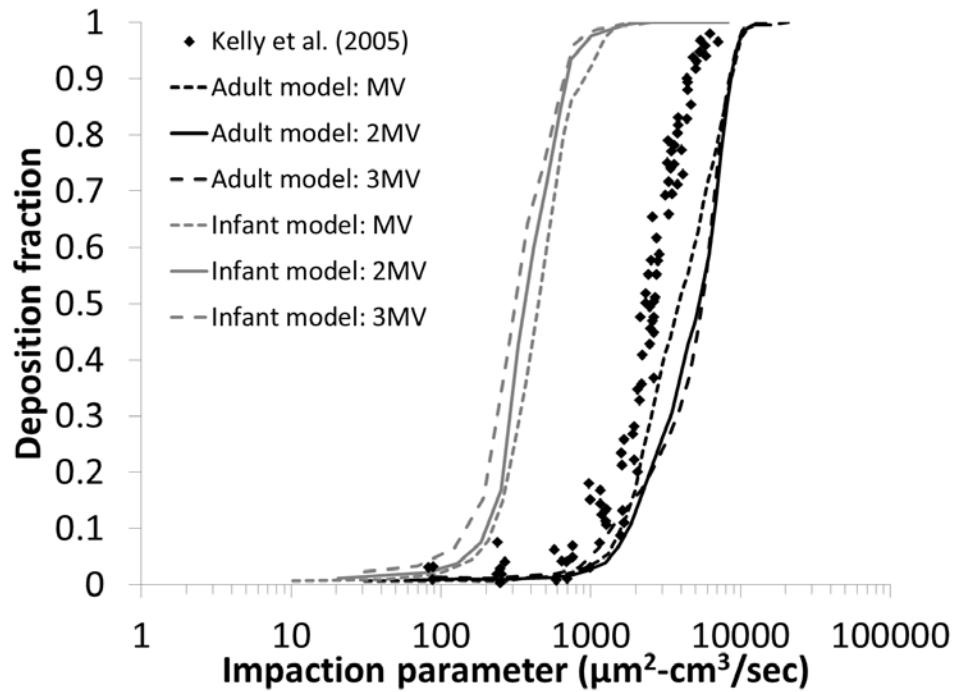
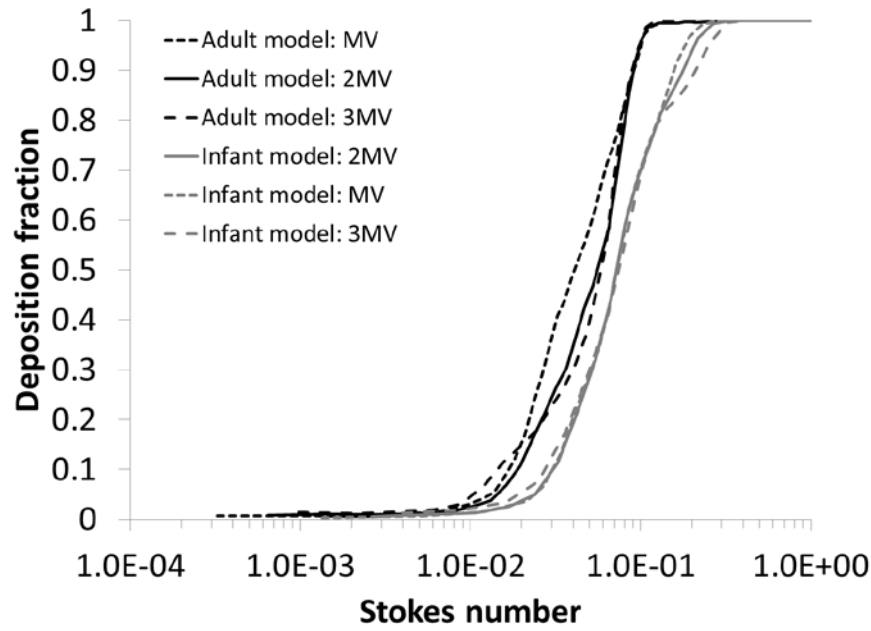


Figure 3-4. Microparticle nasal deposition predictions in the monkey nasal models as a function of particle size - infant model.



**Figure 3-5. Microparticle nasal deposition predictions in the adult and infant monkey nasal models as a function of the impaction parameter. Deposition data from an adult rhesus monkey nasal cast is included (Kelly et al., 2005).**

Nasal deposition fractions in the adult and infant models were also plotted against the Stokes number using various forms of the characteristic diameter from Table 2-2 (Figure 3-6, Figure 3-7, and Figure 3-8, and Figure 3-9). Defining the characteristic diameter to be equal to the hydraulic diameter at the nostrils did not fully account for differences in deposition between the two models (Figure 3-6). Although nostril inlet conditions certainly influence deposition, this form of the characteristic diameter did not account for any downstream differences in model geometry that could also affect the deposition of particles throughout the nose. Use of other forms of the characteristic diameter resulted in a better collapse of the deposition curves when plotted against the Stokes number and were able to account for differences in model size on deposition (Figure 3-6, Figure 3-7, and Figure 3-8). Similar findings were observed by Grgic et al. (2004) and Storey-Bishoff et al. (2008) when accounting for inter-subject variability in human oral airway deposition and infant nasal deposition, respectively. Storey-Bishoff et al. (2008) compared numerous forms of the characteristic diameter and found that the volume-surface ratio definition provided the best collapse of infant nasal deposition data. The characteristic diameter  $d_c = 4 \cdot \text{SAVR}^{-1}$  (SAVR = surface area to volume ratio) was used in further calculations since a good collapse of the data was observed and since nasal volume and surface area can be estimated from body weight and can therefore be used to extrapolate results to other monkey ages (Asgharian et al., 2012).



**Figure 3-6.** Total nasal deposition results of inhaled microparticles in the adult and infant monkey nasal models as a function of Stokes number. Various forms of the hydraulic diameter were used in Stokes number calculations:  $4 \cdot A_{\text{nostril}} / P_{\text{nostril}}$

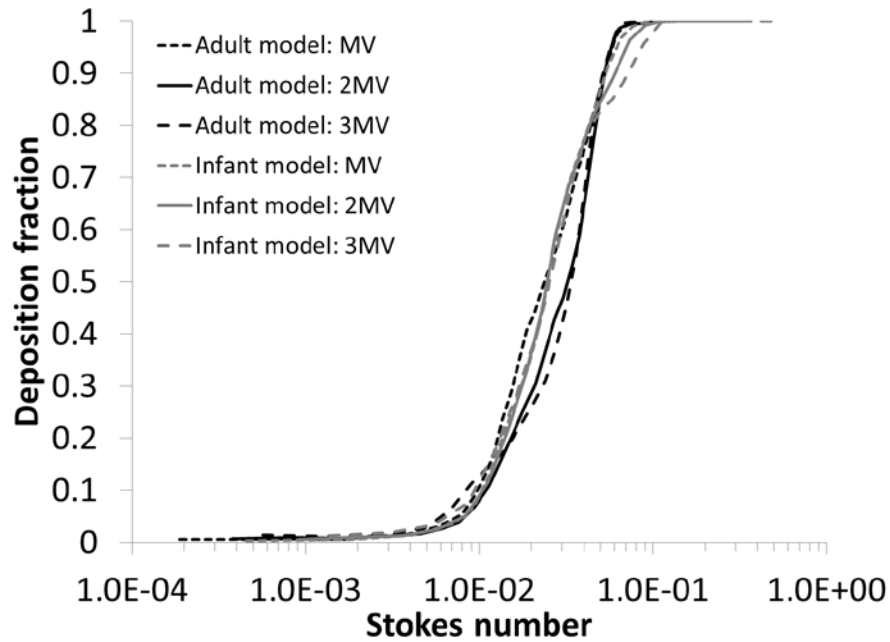


**Figure 3-7.** Total nasal deposition results of inhaled microparticles in the adult and infant monkey nasal models as a function of Stokes number. Various forms of the hydraulic diameter were used in Stokes number calculations:  $2 \sqrt{V / \pi L}$

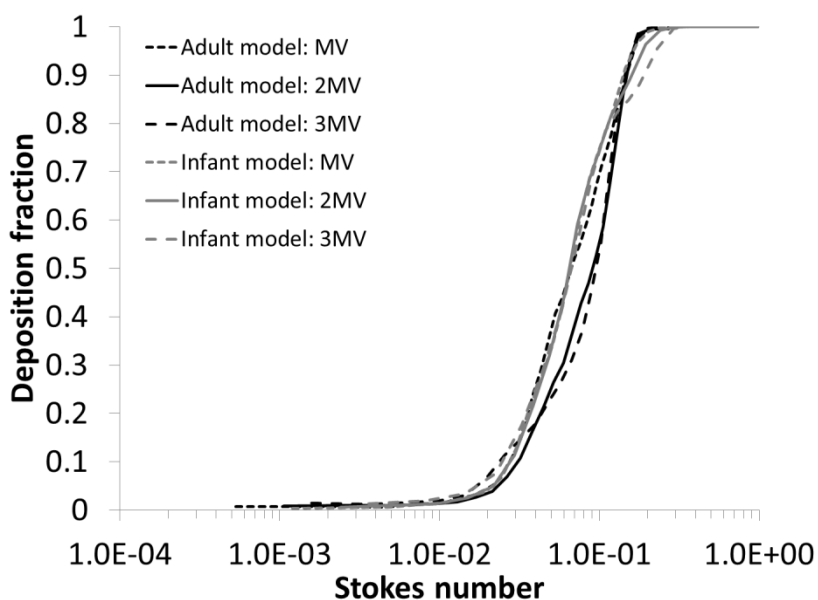


**Figure 3-8. Total nasal deposition results of inhaled microparticles in the adult and infant monkey nasal models as a function of Stokes number. Various forms of the hydraulic diameter were used in Stokes number calculations:  $4 \cdot \text{SAVR}^{-1}$**

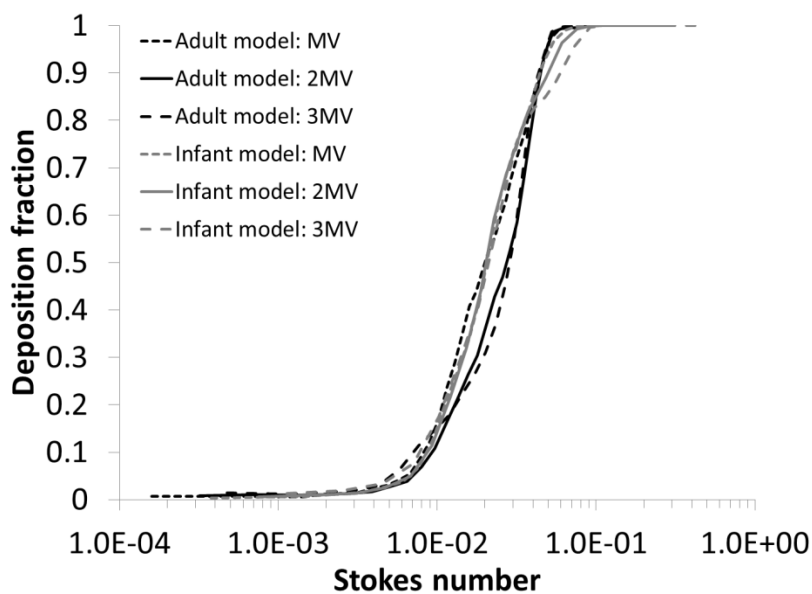


**Figure 3-9. Total nasal deposition results of inhaled microparticles in the adult and infant monkey nasal models as a function of Stokes number. Various forms of the hydraulic diameter were used in Stokes number calculations:  $\sqrt{4A_{cs} / \pi}$**

### 3.3. NASAL NANOPARTICLE DEPOSITION

Nanoparticle simulation results were compared with the experimental data of Yeh et al. (1992), where deposition fractions of 1.7 – 100 nm particles were measured in a replica cast of the nasal airways of an adult rhesus monkey (body weight 8.5 kg). At steady inhalation flow rates of 1.75, 3.5, and 7.0 L/min, Yeh et al. (1992) measured nasal deposition of 1.7 nm particles to range from 78-87% (Figure 3-10). Deposition decreased as particle size increased due to the diminished effects of diffusion. Deposition of 100 nm particles was < 11% at all flow rates. CFD simulations of nanoparticle deposition in the adult rhesus monkey model at flow rates of 1.85, 3.7, and 7.4 L/min compared well with the experimental data (Figure 3-10). A slight under-prediction was observed for particle sizes < 10 nm. This can be partially attributed to the slightly higher flow rates used in the CFD model and the fact that the nasal replica cast used by Yeh et al. (1992) also included the pharynx and larynx.

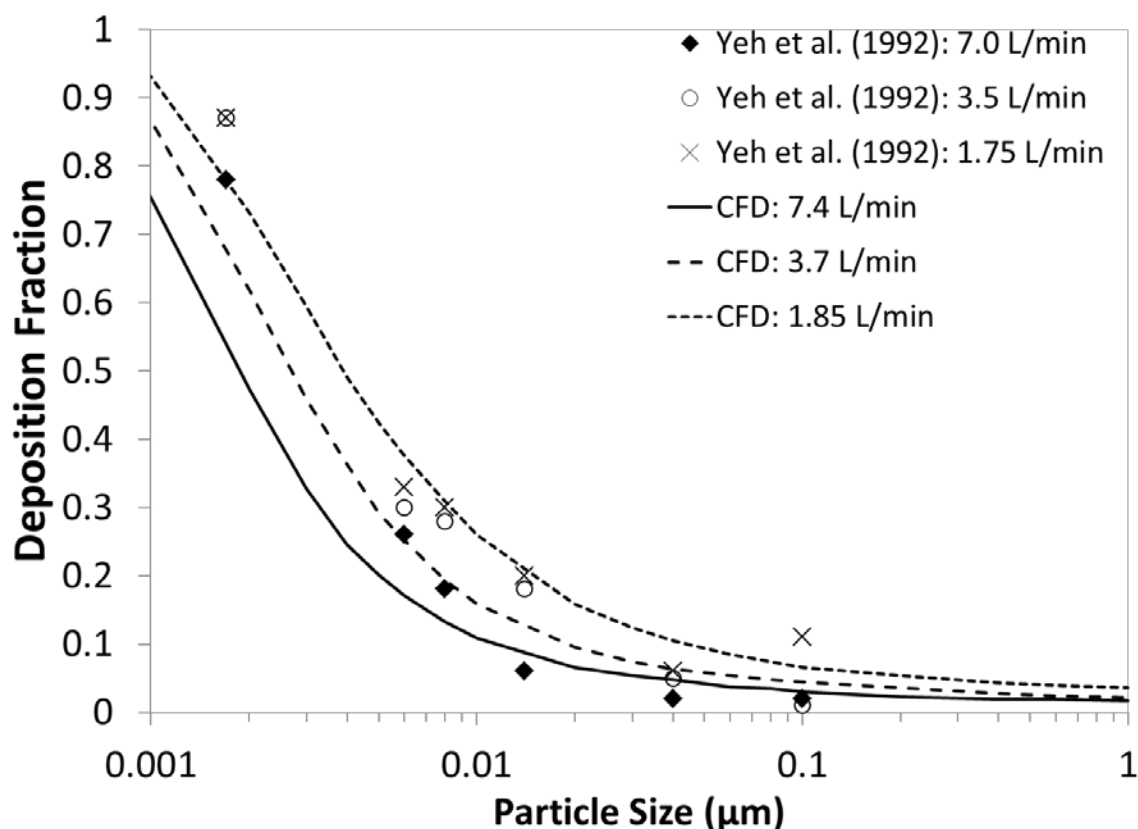


**Figure 3-10. Comparison of nanoparticle deposition predictions in the adult rhesus monkey nasal CFD model with the experimental measurements of Yeh et al. (1992).**

CFD simulations of nanoparticle deposition were conducted in the adult and infant rhesus monkey models at flow rates equal to the MV, 2MV, and 3MV for particle sizes between 0.0005 and 1 μm (0.5 – 1000 nm) (Figure 3-11). At equivalent physiological flow rates, nanoparticle deposition in the infant model was greater than the adult model. For each model, deposition fractions were lower at higher flow



rates due to decreased residence times of nanoparticles in the nasal passages. Deposition of 0.5 nm particles was predicted to be 100% in the infant model at all flow rates. In the adult model, 0.5 nm deposition ranged from 89-99% depending on flow rate. Flow rate differences were most evident for particle sizes < 10 nm. Deposition of 1 nm particles ranged from 65-87% in the adult model and from 91-99% in the infant model. Deposition decreased dramatically as particle size increased to from 1 nm to 10 nm. Deposition of 10 nm particles ranged from 7-16% in the adult model and from 15-28% in the infant model. As particle size increased above 10 nm, deposition slowly decreased further and was < 4% for particle sizes > 100 nm at all flow rates.

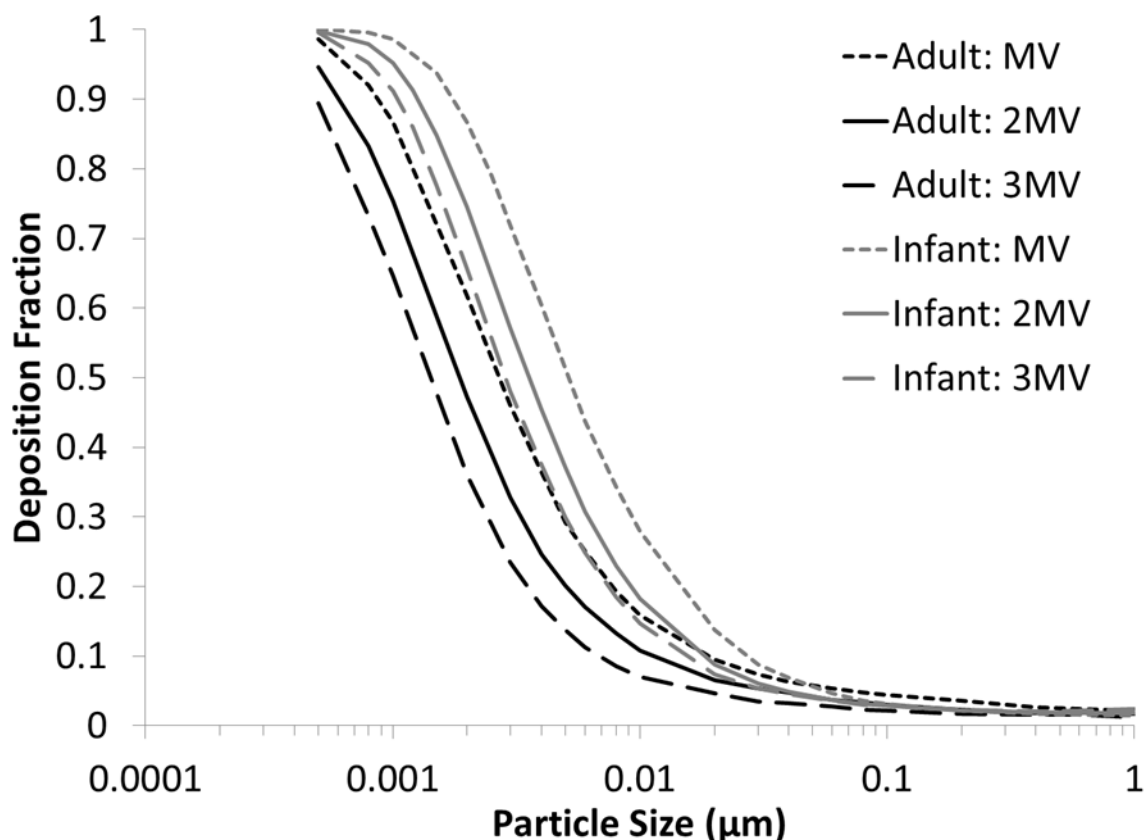


**Figure 3-11. Nanoparticle nasal deposition predictions in the adult and infant monkey nasal CFD models.**

To further compare nanoparticle deposition in the two models, deposition fractions were plotted against the term  $Sc^a \Delta^b$ , where  $a$  and  $b$  are fitted constants. Variability in nanoparticle deposition was reduced considerably with the constants  $a = -0.08$ ,  $b = 0.25$  (Figure 3-12). In this example, the characteristic diameter in the diffusion parameter calculation was defined as  $d_c = 4 \cdot SAVR^{-1}$  to be consistent with the definition in the microparticle deposition results. Because airway dimensions were included in the definitions of the Schmidt number and diffusion parameter, this relationship should apply to a population, assuming that the shape of the nasal passages remains the same but gets larger with age.

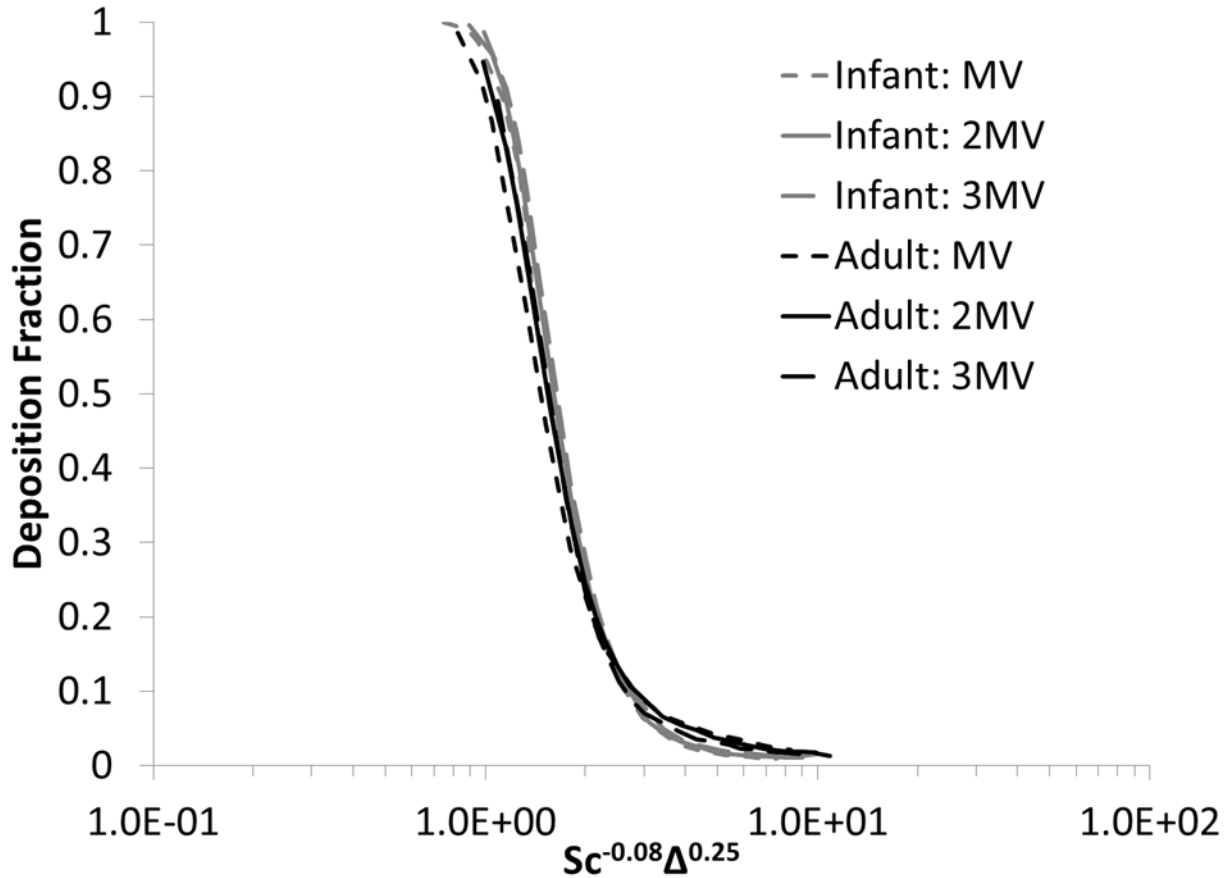


**Figure 3-12. Nanoparticle nasal deposition predictions in the adult and infant monkey nasal CFD models as a function of the diffusion parameter,  $d$ . The characteristic diameter was  $d_c = 2\sqrt{V / \pi L}$ .**

### 3.4. REGIONAL PARTICLE DEPOSITION

Micro- and nano-particle deposition fractions were tabulated for the major nasal epithelial types: squamous, olfactory, and respiratory/transitional epithelia. Deposition was also quantified in the larynx/trachea region of the infant model. Deposition curves for the entire particle size range considered in this study (0.5 nm to 20  $\mu\text{m}$ ) are shown in Figures 3-13 to 3-21. Total nasal deposition curves displayed a classic U-shape that is seen in other species, with high deposition for small nanoparticles and large microparticles (Figure 3-13 and Figure 3-14). Deposition was very low (< 4%) for the fine particle size range of 100 nm to 1  $\mu\text{m}$ . As particle size increased above 1  $\mu\text{m}$ , deposition fractions increased sharply. Similar behavior was observed on squamous epithelia, with moderately high deposition for small nanoparticles and high deposition for large microparticles (Figure 3-15 and Figure 3-16). Deposition of 1 nm particles was predicted to range from 16-36% and from 24-43% in the squamous region in the adult and infant models respectively, depending on flow rate. Nanoparticles diffuse to airway walls upon entering the nasal passages, which leads to enhanced deposition in the anterior section of the nose that is covered by squamous epithelia. Large particles (> 5  $\mu\text{m}$ ) experience deposition by inertial impaction in this region due to high airflow velocities and rapidly changing nasal

shapes. Squamous deposition was higher in the infant model than in the adult model at equivalent physiological flow rates.

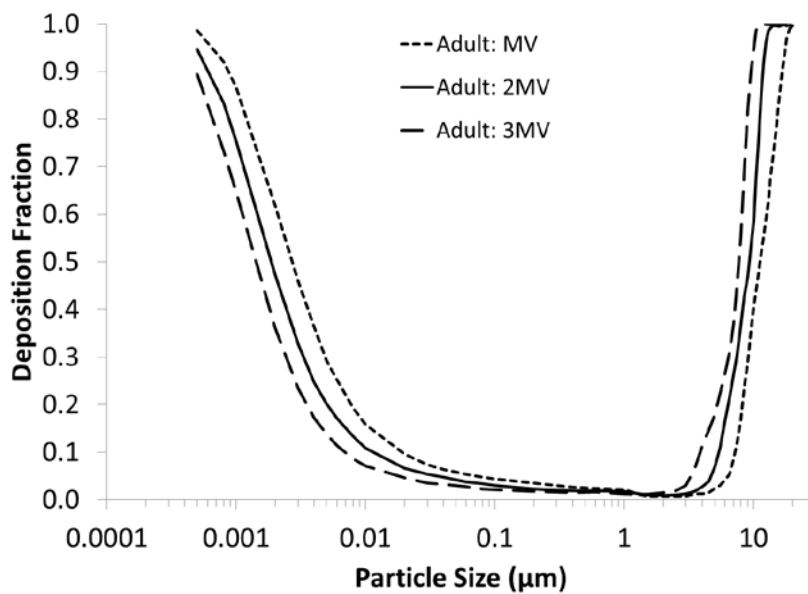


**Figure 3-13. Total nasal deposition predictions in the monkey nasal CFD models: adult.**

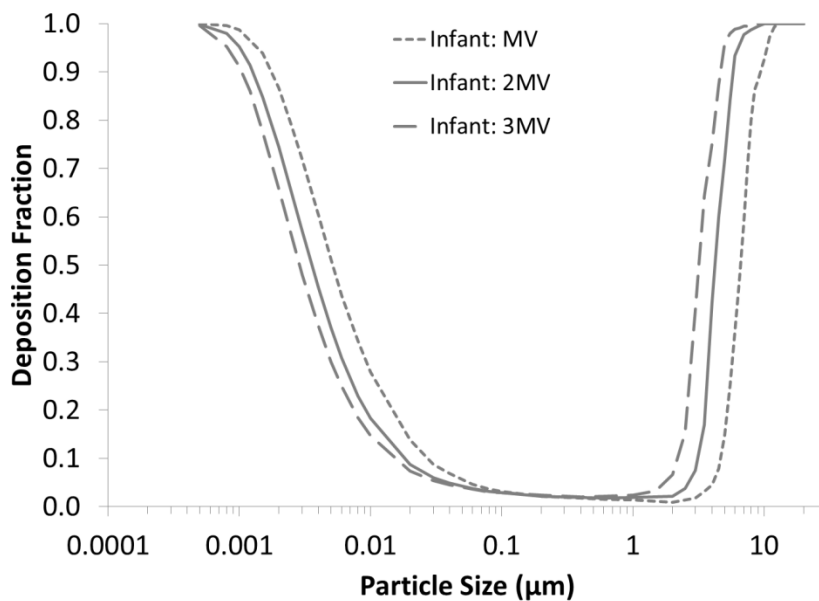


**Figure 3-14. Total nasal deposition predictions in the monkey nasal CFD models: infant.**

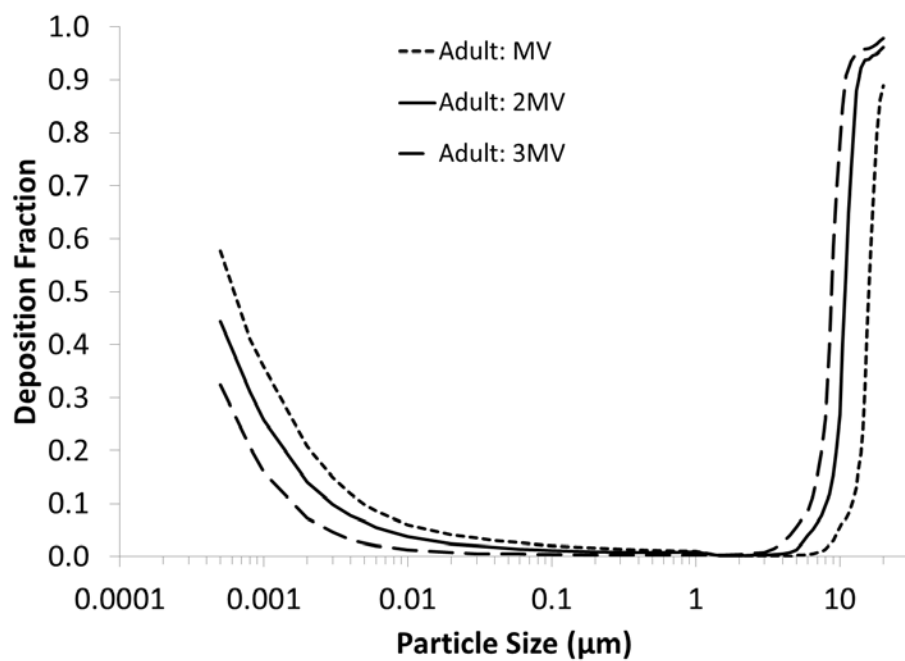


Figure 3-15. Deposition predictions on squamous epithelium in the monkey nasal passages: adult.

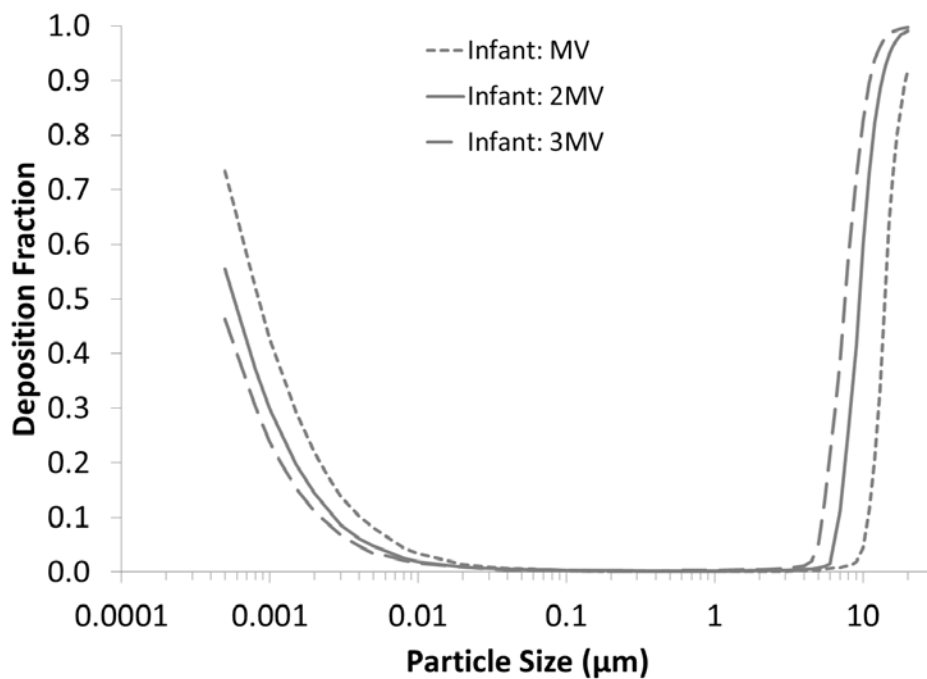
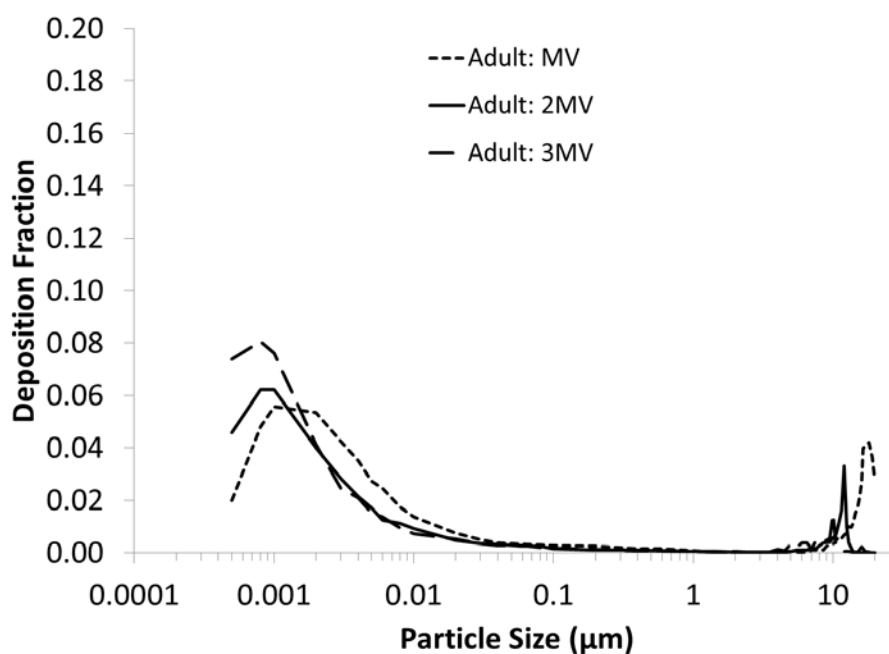
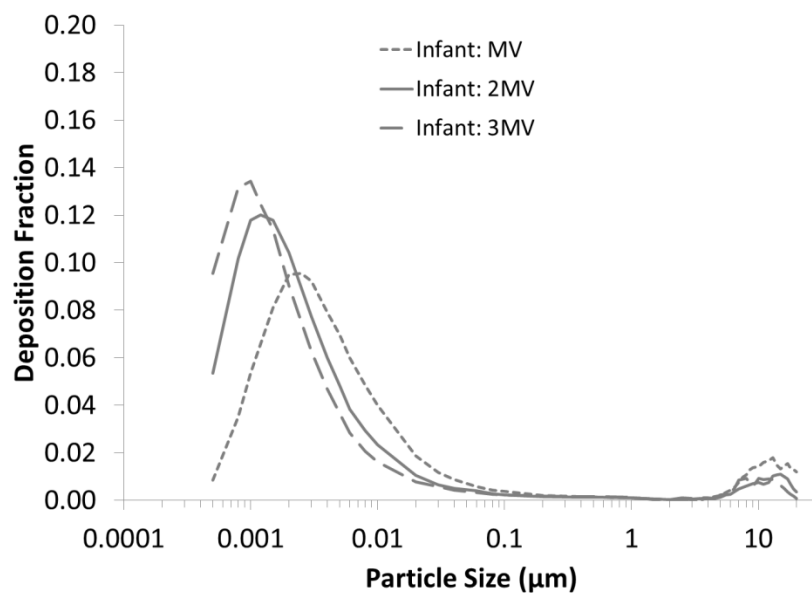


Figure 3-16. Deposition predictions on squamous epithelium in the monkey nasal passages: infant.

Deposition on olfactory epithelium is important to quantify since there is concern for translocation of nanoparticles and certain metals along olfactory neurons to the olfactory bulb (Dorman et al., 2006; Lewis et al., 1994; Oberdoster et al., 2004). In addition, drugs depositing in the olfactory region can be transported to the central nervous system through the olfactory pathway (Thorne et al., 2008). For the particle sizes and flow rates considered in this study, deposition on olfactory epithelium was very low (< 14%). Olfactory deposition displayed a bimodal behavior with higher deposition occurring at very small nanoparticle sizes (< 3 nm) and very large microparticle sizes (> 10  $\mu\text{m}$ ) (Figure 3-17 and Figure 3-18). The highest olfactory deposition in the adult model of 8% occurred at a particle size of 1 nm at the highest flow rate. Nanoparticle olfactory deposition was slightly higher in the infant model with a peak of 14% occurring at a particle size of 1 nm at the highest flow rate. Similar behavior was predicted for particle deposition in the rat nasal passages with the highest olfactory deposition occurring in the 1-3 nm size range (Garcia and Kimbell, 2009; Schroeter et al., 2012). However, this does contrast with predicted olfactory nanoparticle deposition in humans, which was estimated to be < 1% (Shi et al., 2006).



**Figure 3-17. Deposition predictions on olfactory epithelium in the monkey nasal passages: adult.**



**Figure 3-18. Deposition predictions on olfactory epithelium in the monkey nasal passages: infant.**

Deposition on the remaining nasal surface comprised of respiratory and transitional epithelia also displayed a bimodal behavior, with peak deposition occurring at particle sizes of 0.5-2  $\mu\text{m}$  and in the 7-20  $\mu\text{m}$  range (Figure 3-19 and Figure 3-20). Deposition in this region was much higher than in the olfactory region due to the large surface area and higher proportion of airflow passing over these epithelial types.

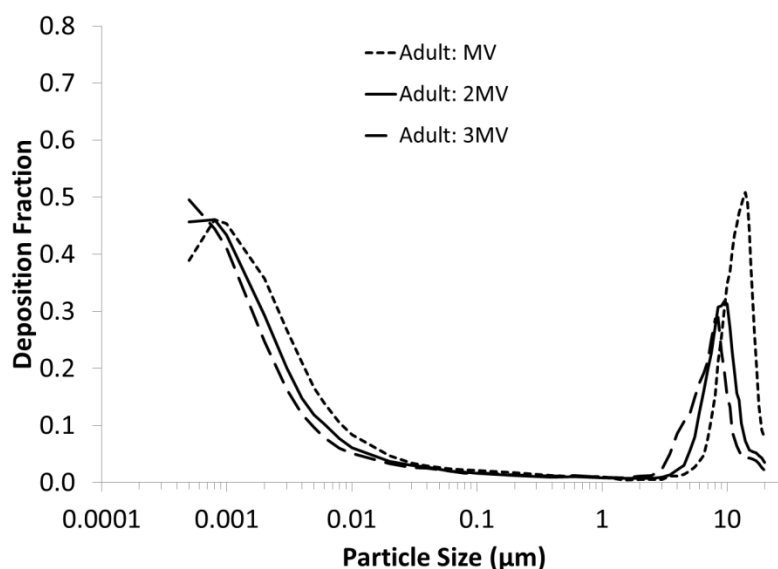


**Figure 3-19. Deposition predictions on respiratory/transitional epithelium in the monkey nasal passages: adult.**

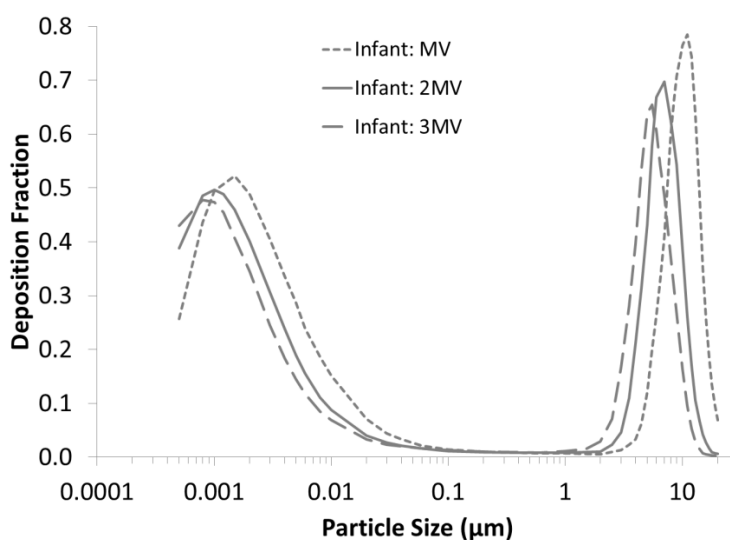


**Figure 3-20. Deposition predictions on respiratory/transitional epithelium in the monkey nasal passages: infant.**

Nanoparticle deposition in the larynx/trachea region of the infant model was < 12% and reached a maximum at a particle size of 2 nm (Figure 3-21). Peak microparticle deposition was significantly higher at 35%, occurring at the highest flow rate at a particle size of 7 μm. Microparticle deposition was

elevated in the larynx area due to the airway constriction resulting in higher airflow velocities in this region, which increases deposition due to impaction.

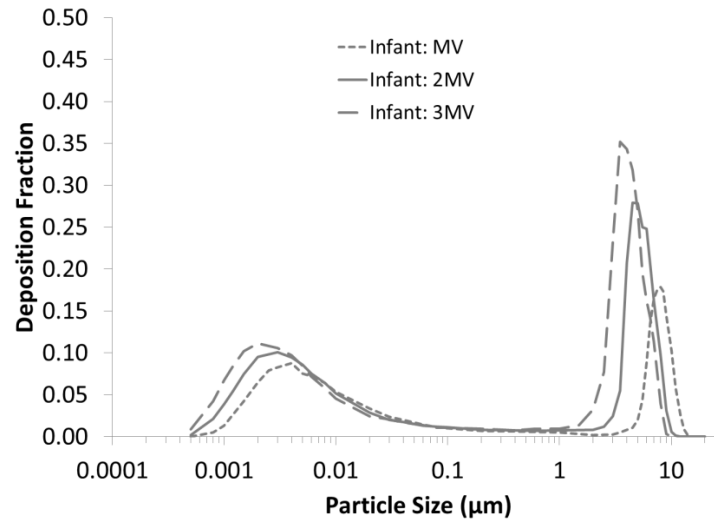


**Figure 3-21. Deposition predictions in the larynx/trachea region in the infant monkey nasal CFD model.**

### 3.5. SEMI-EMPIRICAL NASAL DEPOSITION CURVES

The CFD simulation data was used to develop semi-empirical curves for total nasal deposition. Particle deposition in the upper airways of the respiratory tract directly affects the amount that is available for deposition in the lung. It is desirable to construct analytical relationships for the predicted deposition fraction in the nasal passages as functions of airflow and particle variables that can be implemented in lung deposition models for rhesus monkeys (Asgharian et al., 2012). Two such relationships are needed: one for sub-micrometer-sized particles for which deposition occurs mainly by Brownian diffusion, and also for fine and coarse particles which deposit by inertial impaction in the nasal passages. Deposition by sedimentation is negligible in the upper airways because of small particle residence times.

For micrometer-sized particles, nasal deposition curves collapsed when plotted versus the Stokes number with the characteristic diameter defined in terms of the surface area-volume ratio (Figure 3-7). Likewise, nanoparticle deposition collapsed when plotted as a function of the Schmidt number and diffusion parameter (Figure 3-12). For consistency with the lung geometry model and ease of implementation, deposition efficiencies can also be plotted versus the impaction parameter,  $pd^2Q$ , and in terms of the diffusion coefficient ( $D$ ) and flow rate ( $Q$ ) for microparticles and nanoparticles, respectively. Predicted deposition efficiencies of inhaled particles in the infant nasal passages (which includes deposition in the larynx) were fit to sigmoidal functions as given below:



$$\eta_i = \left( 1 - \frac{1}{1 + \left( \frac{\rho d^2 Q}{B_1} \right)^{C_1}} \right)^{A_1}$$

$$\eta_d = 1 - \frac{F_1}{1 + G_1 \times D^{H_1} Q^{K_1}}$$

where  $\eta_i$  and  $\eta_d$  represent deposition efficiencies by inertial impaction and diffusion, respectively (Figure 3-22 and Figure 3-23). The impaction parameter,  $\rho d^2 Q$ , in the first equation is given in units of  $\text{g} \cdot \mu\text{m}^2/\text{sec}$  while the flow rate,  $Q$ , and diffusion coefficient,  $D$ , in the second equation are given in  $\text{cm}^3/\text{sec}$  and  $\text{cm}^2/\text{sec}$ , respectively. In addition, optimized parameter values for the coefficients are shown in Table 3-1.

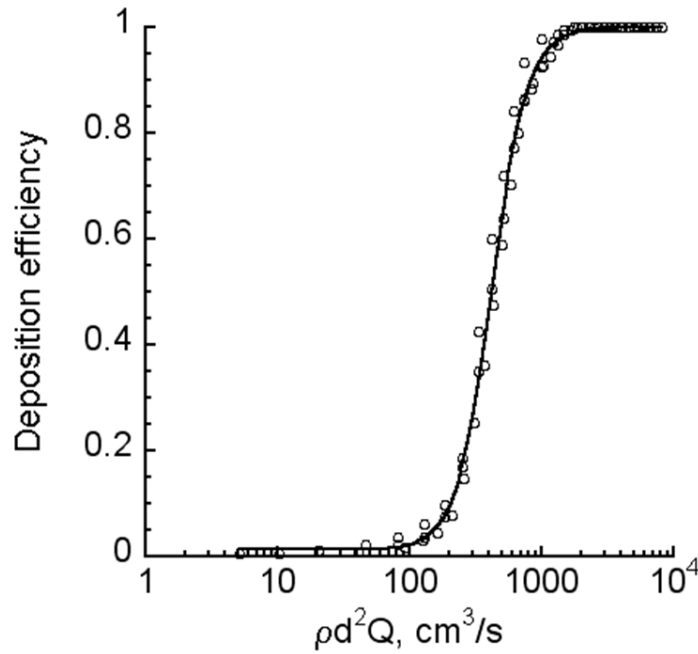


**Figure 3-22. Empirical curve for nasal deposition of microparticles as a function of the impaction parameter. Data points represent CFD simulations results from the infant monkey model.**

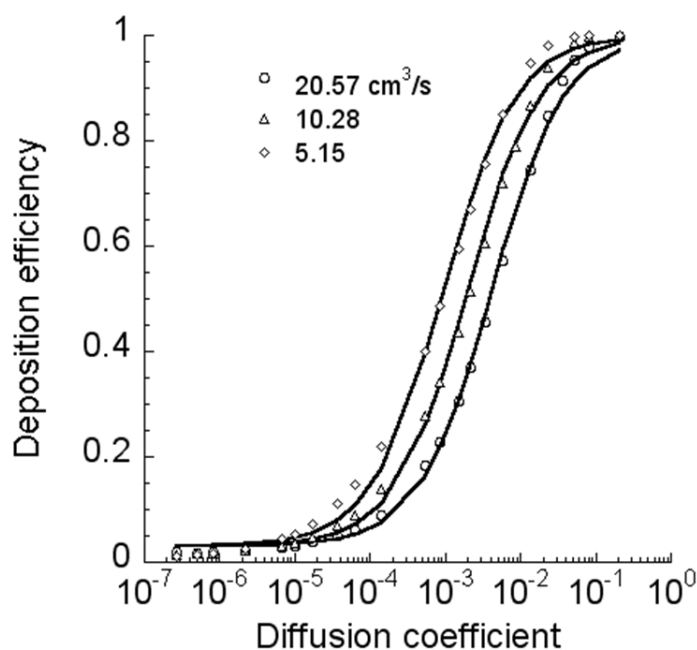


**Figure 3-23. Empirical curves for nasal deposition of nanoparticles as a function of the diffusion parameter. Data points represent CFD simulation results from the infant monkey model.**

**Table 3-1. Optimized parameter values for the sigmoidal functions for nasal deposition by inertial impaction ( $\eta_i$ ) and diffusion ( $\eta_d$ ).**

	Parameter	Value
<b>Impaction (<math>\eta_i</math>)</b>	$A_1$	0.863
	$B_1$	441.540
	$C_1$	3.289
<b>Diffusion (<math>\eta_d</math>)</b>	$F_1$	0.969
	$G_1$	2549.821
	$H_1$	0.901
	$K_1$	-0.958

Assuming that the monkey nasal passages retain their shape during growth and only change in size, the above deposition efficiency formulas may be extended to other ages by correcting for the airway volume and surface areas (Asgharian et al., 2012) to reflect the following change in parameter values:

$$\frac{1}{B_2} = \frac{1}{B_1} \times \left( \frac{S_2/V_2}{S_1/V_1} \right)^3,$$

$$G_2 = G_1 \times \left( \frac{S_2/V_2}{S_1/V_1} \right)^{K_1},$$

where  $S_1$ ,  $V_1$  and  $S_2$ ,  $V_2$  correspond to the nasal surface area and volume of the infant monkey model (see Table 2-1) and a monkey of different age, respectively.

## 4. CONCLUSIONS

CFD models of the nasal passages of an infant and adult rhesus monkey were used to predict deposition of inhaled nanoparticles and microparticles. Nasal deposition was very different between the two models due to their size differences. However, when deposition fractions were plotted against appropriate non-dimensional parameters, the variability between models was substantially reduced. Although only two models were used in this analysis, these results suggest that nasal deposition curves can be extrapolated to rhesus monkeys of other ages assuming that the nasal passages retain their shape with age and that their nasal surface areas and volumes can be measured or estimated. There may be significant inter-individual variability between monkeys that can be explored once other nasal geometries become available.

The semi-empirical nasal filtration equations were implemented into the Multiple-Path Particle Dosimetry (MPPD) lung model that was recently developed for rhesus monkeys (Asgharian et al., 2012). This model can be downloaded at the following address:

<http://www.ara.com/products/mppd.htm>

## 5. WORKS CITED

- Asgharian, B., Price, O., McClellan, G., Corley, R., Einstein, D. R., Jacob, R. E., Harkema, J., Carey, S. A., Schelegle, E., Hyde, D., Kimbell, J. S., and Miller, F. J. (2012). Development of a rhesus monkey lung geometry model and application to particle deposition in comparison to humans. *Inhal. Toxicol.* 24:869-899.
- Bide, R. W., Armour, S. J., and Yee, E. (2000). Allometric respiration/body mass data for animals to be used for estimates of inhalation toxicity to young adult humans. *J. Appl. Toxicol.* 20:273-290.
- Carey, S. A., Minard, K. R., Trease, L. L., Wagner, J. G., Garcia, G. J. M., Ballinger, C. A., Kimbell, J. S., Plopper, C. G., Corley, R. A., Postlethwait, E. M., and Harkema, J. R. (2007). Three-dimensional mapping of ozone-induced injury in the nasal airways of monkeys using magnetic resonance imaging and morphometric techniques. *Toxicol. Pathol.* 35:27-40.
- Cheng, Y. S. (2003). Aerosol deposition in the extrathoracic region. *Aerosol Sci. Technol.* 37:659-671.
- Cheng, Y. S., Irshad, H., Kuehl, P., Holmes, T. D., Sherwood, R., and Hobbs, C. H. (2008). Lung deposition of droplet aerosols in monkeys. *Inhal. Toxicol.* 20:1029-1036.
- Corley, R. A., Kabilan, S., Kuprat, A. P., Carson, J. P., Minard, K. R., Jacob, R. E., Timchalk, C., Glenney, R., Pipavath, S., Cox, T., Wallis, C., Larson, R. F., Fanucchi, M. V., Postlethwait, E., and Einstein, D. R. (2012). Comparative computational modeling of airflows and vapor dosimetry in the respiratory tracts of a rat, monkey, and human. *Toxicol. Sci.* 128:500-516.
- Day, W. C., and Berendt, R. F. (1972). Experimental tularemia in macaca mulatta: Relationship of aerosol particle size to the infectivity of airborne pasteurella tularensis. *Infection and Immunity* 5:77-82.
- Desso, J. M. (1993). The relevance to humans of animal models for inhalation studies of cancer in the nose and upper airways. *Qual. Assur.* 2:213-231.
- Dorman, D. C., Struve, M. F., Wong, B. A., Dye, J. A., and Robertson, I. D. (2006). Correlation of brain magnetic resonance imaging changes with pallidal manganese concentrations in rhesus monkeys following subchronic manganese inhalation. *Toxicol. Sci.* 92:219-227.
- Druett, H. A., Henderson, D. W., Packman, L., and Peacock, S. (1953). Studies on respiratory infection II. The influence of particle size on respiratory infection with anthrax spores. *J. Hyg.* 41:359-371.
- Garcia, G. J. M., and Kimbell, J. S. (2009). Deposition of inhaled nanoparticles in the rat nasal passages: Dose to the olfactory region. *Inhal. Toxicol.* 21:1165-1175.
- Ghalati, P. F., Keshavarzian, E., Abouali, O., Faramarzi, A., Tu, J., and Shakibafard, A. (2012). Numerical analysis of micro- and nano-particle deposition in a realistic human upper airway. *Comp. Biol. Med.* 42:39-49.
- Griffin, T. B., Coulston, F., Wills, H., and Russel, J. C. (1975). Biologic effects of airborne particulate lead on continuously exposed rats and rhesus monkeys. In: *Environmental Quality*

- and Safety. Suppl. Vol. 2. Coulston, F. and Korte, F. (eds.). New York: Academic Press. Pp. 202-220.
- Grgic, B., Finlay, W. H., Burnell, P. K. P., and Heenan, A. F. (2004). In vitro intersubject and intrasubject deposition measurements in realistic mouth-throat geometries. *J. Aerosol Sci.* 35:1025-1040.
- Harkema, J. R. (1991). Comparative aspects of nasal airway anatomy: Relevance to inhalation toxicology. *Toxicol. Pathol.* 19:321-336
- Harper, G. J., and Morton, J. D. (1953). The respiratory retention of bacterial aerosols: Experiments with radioactive spores. *J. Hyg.* 51:372-385.
- Hinds, W. C. (1999). *Aerosol Technology: Properties, Behavior, and Measurement of Airborne Particles*. New York: Wiley-Interscience.
- Hislop, A., Howard, S., and Fairweather, D. V. I. (1984). Morphometric studies on the structural development of the lung in *Macaca fascicularis* during fetal and postnatal life. *J. Anat.* 138:95-112.
- Ingham, D.B. (1991). Diffusion of aerosols in the entrance region of a smooth cylindrical tube. *J. Aerosol Sci.* 22:253-257.
- Jiang, J., and Zhao, K. (2010). Airflow and nanoparticle deposition in rat nose under various breathing and sniffing conditions – A computational evaluation of the unsteady and turbulent effect. *J. Aerosol Sci.* 41:1030-1043.
- Kelly, J. T., Asgharian, B., and Wong, B. A. (2005). Inertial particle deposition in a monkey nasal mold compared with that in human nasal replicas. *Inhal. Toxicol.* 17:823-830.
- Kepler, G. M., Richardson, R. B., Morgan, K. T., and Kimbell, J. S. (1998). Computer simulation of inspiratory nasal airflow and inhaled gas uptake in a rhesus monkey. *Toxicol. Appl. Pharmacol.* 150:1-11.
- Kimbell, J. S., Godo, M. N., Gross, E. A., Joyner, D. R., Richardson, R. B., and Morgan, K. T. (1997). Computer simulation of inspiratory airflow in all regions of the F344 rat nasal passages. *Toxicol. Appl. Pharmacol.* 145:388-398.
- Kimbell, J. S., Subramaniam, R. P., Gross, E. A., Schlosser, P. M., and Morgan, K. T. (2001). Dosimetry modeling of inhaled formaldehyde: Comparisons of local flux predictions in the rat, monkey, and human nasal passages. *Toxicol. Sci.* 64:100-110.
- Klonne, D. R., Ulrich, C. E., Riley, M. G., Hamm, T. E., Morgan, K. T., and Barrow, C. S. (1987). One-year inhalation toxicity study of chlorine in rhesus monkeys (*Macaca mulatta*). *Fundam. Appl. Toxicol.* 9:557-572.
- Lawson, M. J., Craven, B. A., Paterson, E. G., and Settles, G. S. (2012). A computational study of odorant transport and deposition in the canine nasal cavity: Implications for olfaction. *Chem. Senses* 37:553-566.
- Lewis, J. L., Hahn, F. F., and Dahl, A. R. (1994). Transport of inhaled toxicants to the central nervous system: Characteristics of a nose-brain barrier. In: *The Vulnerable Brain and Environmental Risks*, vol. 3: *Toxins in Air and Water* (Isaacson, R. L., Jensen, K. F., eds.). Plenum Press, New York, pp. 77-103.

- Li, A., and Ahmadi, G. (1992). Dispersion and deposition of spherical particles from point sources in a turbulent channel flow. *Aerosol Sci. Technol.* 16:209-226.
- Martonen, T. B., Katz, I. M., and Musante, C. J. (2001). A nonhuman primate aerosol deposition model for toxicological and pharmaceutical studies. *Inhal. Toxicol.* 13:307-324.
- Martonen, T. B., Zhang, Z., Yue, G., and Musante, C. J. (2003). Fine particle deposition within human nasal airways. *Inhal. Toxicol.* 15:283-303.
- Monticello, T. M., Morgan, K. T., Everitt, J. I., and Popp, J. A. (1989). Effects of formaldehyde gas on the respiratory tract of rhesus monkeys: Pathology and cell proliferation. *Am. J. Pathol.* 134:515-527.
- Nikula, K. J., Avila, K. J., Griffith, W. C., and Mauderly, J. L. (1997). Lung tissue responses and sites of particle retention differ between rats and cynomolgus monkeys exposed chronically to diesel exhaust and coal dust. *Fundam. Appl. Toxicol.* 37:37-53.
- Oberdorster, G., Sharp, Z., Atudorei, V., Elder, A., Gelein, R., Kreyling, W., and Cox, C. (2004). Translocation of inhaled ultrafine particles to the brain. *Inhal. Toxicol.* 16:437-445.
- Schroeter, J. D., Kimbell, J. S., Asgharian, B., Tewksbury, E. W., and Singal, M. (2012). Computational fluid dynamics simulations of submicrometer and micrometer particle deposition in the nasal passages of a Sprague-Dawley rat. *J. Aerosol Sci.* 43:31-44.
- Shi, H., Kleinstreuer, C., and Zhang, Z. (2006). Laminar airflow and nanoparticle or vapor deposition in a human nasal cavity model. *J. Biomech. Eng.* 128:697-706.
- Storey-Bishoff, J., Noga, M., and Finlay, W. H. (2008). Deposition of micrometer-sized aerosol particles in infant nasal airway replicas. *J. Aerosol Sci.* 39:1055-1065.
- Thorne, R. G., Hanson, L. R., Ross, T. M., Tung, D., and Frey, W. H. (2008). Delivery of interferon-beta to the monkey nervous system following intranasal administration. *Neuroscience* 152:785-797.
- Yeh, H. C., Cheng, Y. S., Su, Y. F., and Morgan, K. T. (1992). Deposition of radon progeny in nonhuman primate nasal airways. In *Indoor Radon and Lung Cancer: Reality or Myth, Part I*. F. T. Cross, ed. Pp. 235-248. Richland, WA: Battelle Press.
- Yeh, H. C., Muggenburg, B. A., and Harkema, J. R. (1997). In vivo deposition of inhaled ultrafine particles in the respiratory tract of rhesus monkeys. *Aerosol Sci. Technol.* 27:465-470.

## DEFINITIONS, ACRONYMS, AND ABBREVIATIONS

BW	Body Weight
CFD	Computational Fluid Dynamics
CT	Computed Tomography
DTRA	Defense Threat Reduction Agency
Fluent <sup>TM</sup>	CFD software sold by ANSYS, Inc.
ICEM-CFD <sup>TM</sup>	Mesh generation software sold by ANSYS, Inc.
IP	Impaction Parameter
MPPD	Multiple Path Particle Dosimetry
MRI	Magnetic Resonance Imaging
MV	Minute Volume
SAVR	Surface Area to Volume Ratio
SIMPLEC	Method in the Fluent <sup>TM</sup> software
2MV	Twice minute volume
3MV	Three time the minute volume



DISTRIBUTION LIST  
DTRA-TR-15-21

**DEPARTMENT OF DEFENSE**

DEFENSE TECHNICAL INFORMATION CENTER  
8725 JOHN J. KINGMAN ROAD, SUITE 0944  
FT. BELVOIR, VA 22060-6218  
ATTN: DTIC

QUANTERION SOLUTIONS, INC.  
1680 TEXAS STREET, SE  
KIRTLAND AFB, NM 87117-5669  
ATTN: DTRIAC

JOINT PROJECT MANAGER INFORMATION SYSTEMS (JPM IS)  
JOINT PROGRAM EXECUTIVE OFFICE FOR  
CHEMICAL BIOLOGICAL DEFENSE (JPEO-CBD)  
301 PACIFIC HIGHWAY  
SAN DIEGO, CA 92110

DEFENSE THREAT REDUCTION AGENCY  
8725 JOHN J. KINGMAN ROAD  
FT. BELVOIR, VA 22060-6201  
ATTN: DR. CHRISTOPHER KILEY /J9CBA

DEFENSE THREAT REDUCTION AGENCY  
8725 JOHN J. KINGMAN ROAD  
FT. BELVOIR, VA 22060-6201  
ATTN: MR. JERRY GLASOW /J9CBI

DEFENSE THREAT REDUCTION AGENCY  
8725 JOHN J. KINGMAN ROAD  
FT. BELVOIR, VA 22060-6201  
ATTN: MR. RICHARD FRY /J9CBI

DEFENSE THREAT REDUCTION AGENCY  
8725 JOHN J. KINGMAN ROAD  
FT. BELVOIR, VA 22060-6201  
ATTN: MR. THOMAS WOLFINGER /J9CBI

DEFENSE THREAT REDUCTION AGENCY  
8725 JOHN J. KINGMAN ROAD  
FT. BELVOIR, VA 22060-6201  
ATTN: DR. ERIN REICHERT /J9CBM

DEFENSE THREAT REDUCTION AGENCY  
8725 JOHN J. KINGMAN ROAD  
FT. BELVOIR, VA 22060-6201  
ATTN: DR. RON MERIS /J9ISR

DEFENSE THREAT REDUCTION AGENCY  
8725 JOHN J. KINGMAN ROAD  
FT. BELVOIR, VA 22060-6201  
ATTN: DR. AIGUO WU /J9ISR

**DEPARTMENT OF DEFENSE CONTRACTORS**

APPLIED RESEARCH ASSOCIATES, INC  
SECURITY ENGINEERING AND APPLIED SCIENCES  
119 MONUMENT PLACE  
VICKSBURG, MS 39180-5156  
ATTN: MR. JOSEPH L. SMITH